energies

MDPI

Article

Heat Transfer and Flow Characteristics of Bidirectional Curved Wavy Microchannels

Jiali Zhang [1], Guangyi Shao [2] and Bo Wang [2,*]

[1] Hangzhou Join Electric Technology Co., Ltd., Hangzhou 310030, China; jiali.zhang@joinelectric.com
[2] School of Energy and Power Engineering, University of Shanghai for Science and Technology, Shanghai 200093, China; shaogy0815@163.com
* Correspondence: wangbo@usst.edu.cn

Abstract

Compared with straight microchannels, wavy microchannels have been shown to significantly improve the heat transfer capability of microchannel heat sinks. The present study introduces a bidirectional curved wavy microchannel design aimed at enhancing performance. The thermo-hydraulic performance of bidirectional curved and ordinary wavy microchannels within the Reynolds number range of 300–800 is analyzed numerically under a constant heat flux. The results indicate that the bidirectional curved microchannel achieves optimal performance at an inlet velocity of 0.6 m/s. Compared with the ordinary wavy microchannel, the comprehensive performance factor of the bidirectional curved wavy microchannel with A_2 = 2 mm and λ_2 = 8 mm increases by 48% under the same inlet Reynolds number. For the preferred bidirectional curved wavy microchannel with A_2 = 2 mm and λ_2 = 12 mm, the average secondary flow intensity is enhanced by 153%, the comprehensive performance factor reaches 1.35, and the minimum entropy generation rate decreases by 6.87%. The enhanced heat transfer is attributed to the increased main flow velocity and the secondary flow intensity due to the bidirectional curve, which promotes coolant mixing.

Keywords: bidirectional curved wavy microchannel; thermo-hydraulic performance; secondary flow

Academic Editor: Marco Marengo

Received: 22 May 2026
Revised: 20 June 2026
Accepted: 25 June 2026
Published: 26 June 2026

Copyright: © 2026 by the authors. Licensee MDPI, Basel, Switzerland. This article is an open access article distributed under the terms and conditions of the Creative Commons Attribution (CC BY) license.

1. Introduction

In recent years, advancements in technology and increasing demand have placed greater emphasis on high-performance and safe thermal solutions. This demand is particularly prominent in the fields of electronic equipment cooling [1] and power battery thermal management [2]. The concept of microchannels was first proposed by Tuckerman and Pease [3]. Microchannel heat sinks are valued for their superior heat dissipation capabilities, withstanding heat fluxes of up to approximately 100 W/cm^2, and offering advantages such as small size, light weight, compactness, and low coolant requirements [4]. In traditional straight microchannels, heat transfer performance diminishes over time due to the thickening of the flow boundary layer, leading to a larger temperature gradient across the channels, especially under high heat fluxes. When fluid flows through a curved pipe at sufficient velocity, centrifugal force generates secondary vortices in the transverse plane. These vortices enhance fluid mixing and heat transfer. Inspired by these vortices, researchers have explored various types of curved microchannels.

Sui et al. [5] proposed a sinusoidal wavy microchannel and compared it with the conjugate heat-transfer simulation of an ordinary straight microchannel subjected to uniform heat flux and constant wall-temperature boundary conditions. Later, Sui et al. [6] conducted experimental investigations into the flow friction and heat transfer characteristics of rectangular sinusoidal microchannels, and verified the comprehensive enhancement effect of sinusoidal microchannels. Moreover, the results also indicated that both the number and spatial distribution of vortical structures can vary throughout the channel, leading to chaotic advection, which significantly enhances convective mixing within the working fluid. It was also suggested that the wave-amplitude ratio of the microchannel along the flow direction could be adjusted based on actual heat dissipation needs, effectively addressing local overheating issues. Similarly, M. Khoshvaght-Aliabadi et al. [7] performed experimental assessments on the thermal–hydraulic characteristics of wavy microchannel heat sinks. Their results showed a superior heat-removal capability for wavy microchannel heat sinks when compared with conventional straight-channel heat sinks. M. Khoshvaght-Aliabadi et al. [8] and Lin et al. [9] further developed a variable-geometry wavy-channel configuration, in which the wavelength decreases or amplitude increases along the flow direction. This design exhibited reduced thermal resistance together with a more homogeneous temperature distribution on the bottom wall. Some studies have also demonstrated the effects of wave amplitude and wavelength on overall channel thermal–hydraulic behavior [10–13]. Various channel shapes, including zigzag, curvy, and step, have been investigated to identify the optimal heat sink design [14,15]. Among these, zigzag channels consistently demonstrate enhanced heat-transfer capability relative to other non-straight channel geometries. Sharma and Khan [16] evaluated and compared the thermo-hydraulic characteristics of elliptical-wavy and sinusoidal-wavy microchannels and found that elliptical-wavy microchannels generally exhibit better thermo-hydraulic performance than sinusoidal-wavy microchannels across most models.

In addition to microchannels employing parallel wavy sidewalls, microchannels can also be designed with converging–diverging symmetric wavy walls [17–19]. However, symmetric wavy ones generally exhibit inferior thermal performance relative to their parallel-wall counterparts. Then, Zhu et al. [20] combined symmetric sinusoidal sidewalls with rectangular rib structures in microchannels. Hasis et al. [13] proposed a twisted sinusoidal wavy microchannel. To address the limitations of wavy microchannels in compact structures, Zhang et al. [21] introduced a curved wavy-channel configuration. In addition to studies focusing on the structural characteristics of wavy microchannels themselves, there has also been extensive research on wavy microchannel heat sinks. Numerical studies conducted by Hung et al. [22] demonstrated that double-layered microchannel heat sinks exhibit superior thermal performance compared with their single-layer counterparts, with an average enhancement of 6.3%. Xie et al. [23] pointed out that a double-layer wavy microchannel heat sink can simultaneously enhance heat transfer capability and decrease flow-resistance losses relative to a single-layer wavy design. Moreover, double-layered microchannel heat sinks with a counter-flow configuration provide more uniform cooling performance than those operating under parallel-flow arrangements [24]. Additionally, to address the design challenges associated with employing either upper–lower or left–right wave patterns in microchannel heat sinks, Zhu et al. [25] investigated the variations in total thermal resistance together with the peak bottom-wall temperature of these two distinct wavy-channel configurations under constant-pumping-power conditions. The differences in heat transfer performance between the two designs at small wavelengths are attributed to the distinct positions of the generated Dean vortices.

In the field of thermal management for cylindrical lithium-ion batteries, wavy microchannels have attracted significant attention because of their ability to conform to battery curvature, enlarge the heat transfer area, and enhance cooling performance. Guo et al. [26]

demonstrated that a counter-flow parallel dual-tube configuration significantly improved temperature uniformity compared with a single long tube. Tang et al. [27] experimentally showed that increasing the contact angle and coolant flow rate effectively reduced both the maximum temperature and temperature difference in battery modules. However, most existing wavy microchannels employ unidirectional bending structures, resulting in a gradual deterioration of cooling capacity along the flow direction due to the continuous temperature rise of the coolant. To overcome this limitation, Yogeshwar et al. [28] proposed a double-serpentine cold plate, which achieved lower peak temperatures and improved temperature uniformity compared with conventional single-serpentine designs.

Building upon previous research, the present study developed a bidirectional wavy microchannel heat sink with similar configuration to Yogeshwar et al.'s [28] design for enhanced thermal management of battery modules. Compared to existing solutions, the proposed structure exhibits significant advantages including simplified architecture, enhanced design flexibility, and improved manufacturability. To conduct preliminary evaluation of the heat sink's comprehensive performance, this work primarily focuses on investigating the thermal–hydraulic characteristics of individual bidirectional undulating microchannels within the cooling system.

2. Numerical Methodology

2.1. Physical Model

The microchannel heat sink under investigation (Figure 1b) is created by rolling a flat plate heat sink containing an embedded up–down wavy flow channel (Figure 1a). Cylindrical lithium batteries can be placed on both sides of the heat sink, as shown in Figure 1c. For this heat sink, it is assumed that the heat dissipation performance of each flow channel is consistent, and the structure of the flow channel has the greatest influence on its performance. Studying the performance of the flow channel micro-element can provide reference values for the form design of the entire heat sink.

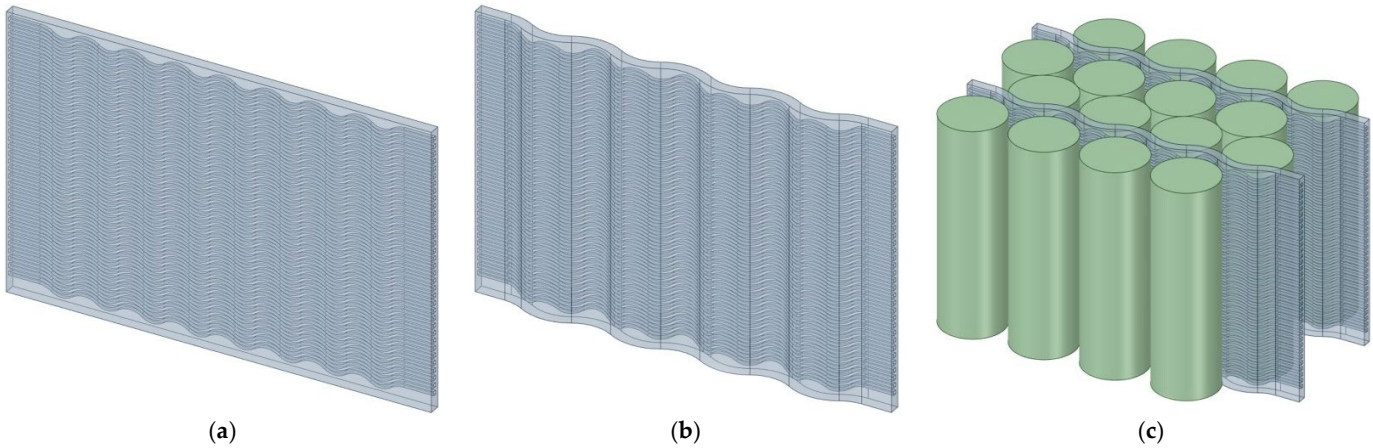

(**a**) (**b**) (**c**)

Figure 1. (**a**) Ordinary wavy microchannel plate heat sink; (**b**) bidirectional curved wavy microchannel plate heat sink; (**c**) bidirectional curved wavy microchannel plate heat sink combined with cylindrical lithium battery.

In addition, considering the geometric periodic arrangement of the channel elements, only one unit is modeled as the computational domain and the upper and lower walls are periodic boundary conditions. Figures 2a and 2b show the physical models of a single ordinary wavy microchannel and a bidirectional curved wavy microchannel (BCWM), respectively. As shown in Figure 2b, the bidirectional curved wavy microchannel features waveform fluctuations in both the horizontal and vertical directions simultaneously, whereas the ordinary wavy microchannel typically exhibits fluctuations only in the

horizontal direction. The solid substrate of the microchannel is made of aluminum. The walls of the wavy section in the middle of the microchannel are heated on both sides. The *x*-*z* planes of both channels are shown in Figure 2c. The channel consists of a straight segment of 8 mm at both ends and a wavy segment of 96 mm in the middle. The straight channel enhances calculation accuracy and helps prevent backflow during the simulation process. The wavelength (λ_1) and amplitude (A_1) of the bidirectional curved wavy microchannel in the horizontal direction are 24 mm and 3.22 mm (according to the 21700 lithium-ion battery size design), respectively. Since A_1 and λ_1 are determined by the diameter of the cylindrical battery and the magnitude of the contact angle, in this study the diameter is fixed at 21 mm and the contact angle at 60°, so A_1 and λ_1 are kept constant. The vertical fluctuation of the bidirectional curved wavy microchannel is illustrated in Figure 2d. The wavelength (λ_2), amplitude (A_2), and wavelength-to-amplitude ratio (γ_2) in the vertical direction are 12 mm, 2 mm, and 6, respectively. The inlet section of the channel is depicted in Figure 2e. The fluid flow channel measures 1 mm × 1 mm, with wall thicknesses of 1 mm on the left and right sides, and 0.5 mm on the top and bottom surfaces. Additionally, this study focuses exclusively on the thermo-hydraulic performance of the intermediate heated section.

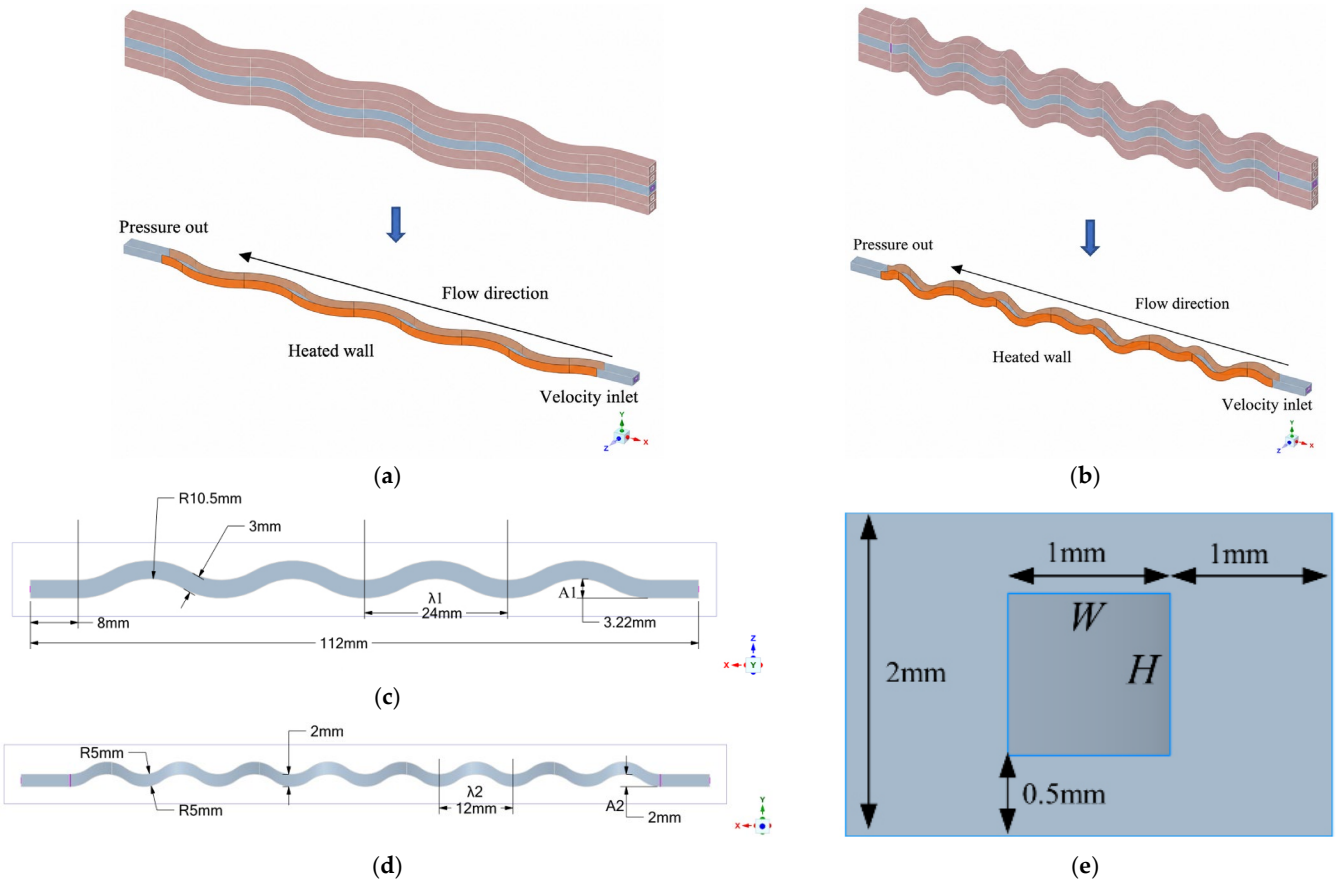

Figure 2. (**a**) Ordinary wavy microchannel; (**b**) bidirectional curved wavy microchannel; (**c**) *x*-*z* plane diagram of ordinary wavy microchannel and bidirectional curved wavy microchannels; (**d**) *x*-*y* plane diagram of bidirectional curved wavy microchannel with A_2 = 2 mm and λ_2 = 12 mm; (**e**) inlet cross-section.

2.2. Numerical Simulation and Boundary Conditions

The fluid considered in this study is water, flowing in a stable laminar state within the microchannel. Natural convection and radiation heat transfer within the channel are neglected. Based on these assumptions, the governing equations for flow and heat transfer are formulated as follows:

Continuity equation:

$$\nabla U = 0 \tag{1}$$

Momentum equation:

$$\rho(U \cdot \nabla U) = -\nabla p + \nabla \cdot (\mu \cdot \nabla U) \tag{2}$$

Energy equation in the flow domain:

$$\rho c_p\left(U \cdot \nabla T_f\right) = \lambda_f \nabla^2 T_f \tag{3}$$

Energy equation in the solid domain:

$$\lambda_s \nabla^2 T_s = 0 \tag{4}$$

In Equations (1)–(4), subscripts f and s represent the fluid and solid, respectively, U is the fluid velocity vector in unit of m/s, T is temperature in unit of K, μ is the viscosity in unit of Pa·s, ρ is the density in unit of kg/m^3, and c_p is the specific heat capacity in unit of J/(kg·K).

The boundary conditions are as follows.

For the entire channel inlet:

$$u = U_{in};\ v = w = 0;\ T_f = T_{in} = 293.15\ \mathrm{K} \tag{5}$$

For the entire channel outlet:

$$P_{out} = 1\ \mathrm{atm} \tag{6}$$

All fluid–solid interfaces are specified as no-slip boundaries with conjugate heat-transfer conditions.

When the battery is integrated with a heat sink, the heat flux distribution on the heated surface is inherently non-uniform. Since the primary purpose of this work is to investigate the effects of different microchannel configurations, a uniform heat-flux boundary condition is adopted for simplification. It is assumed that two rows of batteries are symmetrically arranged on each side of the cold plate for heat dissipation. The heat generation of a single 21700 lithium-ion cell is approximately 4 W; therefore, the total thermal load generated by four cells is 16 W. The effective heat dissipation area on one side of the radiator is approximately 0.00754 m^2. Based on these parameters, the average wall heat flux is estimated to be 2500 W/m^2. The wall of the middle heated section is subjected to a constant heat flux:

$$q_w = 2500\ \mathrm{W/m^2} \tag{7}$$

Adiabatic boundaries are applied to other surfaces.

The following variables are presented in order to comprehensively evaluate the thermo-hydraulic performance of the microchannel.

The Reynolds number is expressed as

$$Re = \frac{\rho_f U D}{\mu} \tag{8}$$

where D represents the hydraulic diameter of the channel inlet cross-section, and it is given by

$$D = \frac{2WH}{(W + H)} \tag{9}$$

The average velocity of the fluid in the heated section:

$$U = \frac{(U_{\text{in}} + U_{\text{out}})}{2} \tag{10}$$

where U_{in} and U_{out} are the area-weighted average velocity at the inlet and outlet of the channel in the heated section, respectively.

The Nusselt number (Nu) is a dimensionless number describing the convective heat transfer intensity and an index to evaluate the heat transfer performance of fluid, and it is given by

$$Nu = \frac{hD}{\lambda_f} \tag{11}$$

where h is the average convective heat transfer coefficient, and λ_f is the thermal conductivity of the fluid.

For the constant-heat-flux condition case, the average heat transfer coefficient is given by

$$h = \frac{q_w A_{\text{w}}}{A_{con}(T_{con,ave} - T_{f,ave})} \tag{12}$$

where A_{w} is the heated surface area of the computational model; A_{con} is the area of the interfaces that coupling the fluid domain and solid domain in the heated section; $T_{con,ave}$ is the average temperature of these interfaces in the heated section; $T_{f,ave}$ is the average temperature of fluid domain in the heated section, and it is given by

$$T_{f,ave} = \frac{T_{f,in} + T_{f,out}}{2} \tag{13}$$

where $T_{f,in}$ and $T_{f,out}$ are the mass-weighted average temperature of the fluid flow at the inlet and outlet of the heated section channel.

q_m is the mass flow rate of the channel, which is defined as

$$q_m = AU\rho_f \tag{14}$$

where A is the channel cross-section area.

The local Nusselt number is defined as

$$Nu_x = \frac{h_x D}{\lambda_f} \tag{15}$$

For the constant-heat-flux condition case, the local heat transfer coefficient of the heated section is given by

$$h_x = \frac{q_w A_{\text{w}}}{A_{\text{con}}(T_{con,x} - T_{f,x})} \tag{16}$$

where $T_{con,x}$ is the perimeter averaged wall surface temperature, and $T_{f,x}$ represents the mass-weighted average temperature of local cross-section fluid.

The Darcy friction coefficient (f) is a dimensionless index used to evaluate the pressure loss, defined as

$$f = \frac{2\Delta pD}{\rho_f U^2 L} \tag{17}$$

The pressure-drop loss of the fluid is defined as

$$\Delta p = p_{\text{in}} - p_{\text{out}} \tag{18}$$

where p_{in} and p_{out} are the area-weighted average pressure at the inlet and outlet of the heated section of the channel, and L is the length of the flow channel in the heated section.

To assess the overall thermo-hydraulic performance of bidirectional curved wavy microchannels by considering both heat transfer enhancement and the associated pressure-drop penalty, the performance evaluation criteria (η) proposed by Webb [29] is adopted as an indicator of the overall performance of the heated section under constant-pumping-power conditions. The criterion is defined as follows:

$$\eta = \frac{Nu/Nu_0}{(f/f_0)^{(1/3)}} \tag{19}$$

where subscript 0 represents the ordinary wavy microchannel in this study.

2.3. Grid Independency Test

In this study, the commercial software ANSYS Fluent 2020R1 was employed to solve the governing equations. The SIMPLE algorithm was used to determine the velocity and pressure fields within the microchannel. Pressure discretization was handled using the standard scheme, while the momentum and energy equations were discretized with a second-order upwind scheme. The computations were considered converged when the residuals for continuity and energy fell below 1×10^{-8} and 1×10^{-10}, respectively.

This study employs the advanced preprocessing module Fluent Meshing within Ansys Fluent for mesh generation. The overall model is meshed using the Polyhedra method to generate volumetric grids, with boundary layer refinement applied to near-wall regions, setting the number of boundary layers to five. The minimum orthogonal quality of the mesh is 0.22, and the maximum skewness is 0.77, indicating good mesh quality. Taking the bidirectional curved wavy microchannel with A_2 = 2 mm and λ_2 = 12 mm as an example, under the constant-heat-flux boundary condition with an inlet velocity of 0.8 m/s, an inlet fluid temperature of 293.15 K, and a heat flux density of 2500 W/m^2, the variation in the Nusselt number with the number of grids obtained from numerical simulation is shown in Figure 3. The results indicate that when the grid number reaches 1.72 million, the relative error of the Nusselt number compared to that obtained with 2.54 million grids is only 0.18%, satisfying the grid independence requirement.

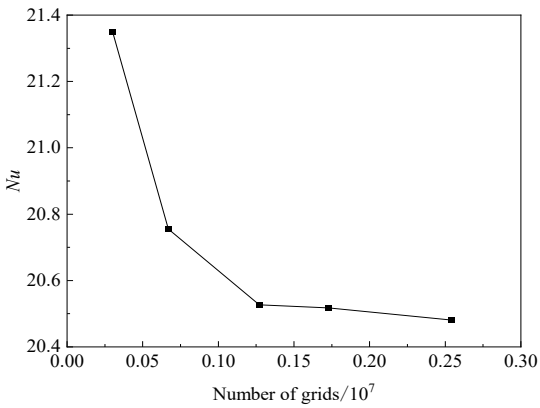

Figure 3. Grid independence test.

2.4. Model Validation

Currently, although there are numerous experimental results on the thermo-hydraulic performance of straight channels and ordinary wavy microchannels, no experimental studies have been conducted on bidirectional curved wavy microchannels. Hasis et al. [13] proposed a twisted wavy microchannel, and due to the similarity in flow dynamics between their study and the current research, the experimental data from Sui et al. [6] on sinusoidal microchannels with rectangular cross-sections were selected for validation. Given the resemblance between the model in this study and the flow characteristics of twisted wavy microchannels and sinusoidal microchannels, the experimental data for sinusoidal microchannels with rectangular cross-sections are also used to validate the model.

As shown in Figure 4a, a relatively large discrepancy between the simulated Nusselt number (*Nu*) and the experimental results is observed at high Reynolds numbers (*Re*). The

maximum deviations between numerical predictions and experimental data are 31% for *Nu* at *Re* = 800 and 13% for the friction factor at *Re* = 300, while the corresponding average deviations are 13.8% and 6.3%, respectively. These discrepancies can be attributed to several factors. First, experimental uncertainties in measuring wall and fluid temperatures, as well as geometric dimensions of the microchannel, may introduce unavoidable errors. At high Reynolds numbers, a more pronounced temperature gradient develops within the fluid, which further amplifies measurement sensitivity and contributes to the deviation in the Nusselt number. The deviation in the friction factor at low Reynolds numbers, as shown in Figure 4b, can be explained by the relatively stronger influence of surface roughness under low-inertia flow conditions. In addition, at low *Re*, the inlet region effect becomes more significant, since the flow may not yet be fully developed. Moreover, the deviations may also be partly attributed to the limitations of the laminar flow model in capturing flow disturbances, deviation from ordered flow structures, and loss of periodicity in wavy channels at higher Reynolds numbers.

Overall, the simulation results show good agreement with the experimental data, indicating that the numerical model provides reasonable accuracy for predicting the thermo-hydraulic performance of wavy microchannels. This validation primarily serves as a general verification of the flow and heat transfer modeling approach in three-dimensional curved microchannels. Due to the lack of experimental data for BCWM, further experimental investigations are required in future work to provide additional validation of the proposed model.

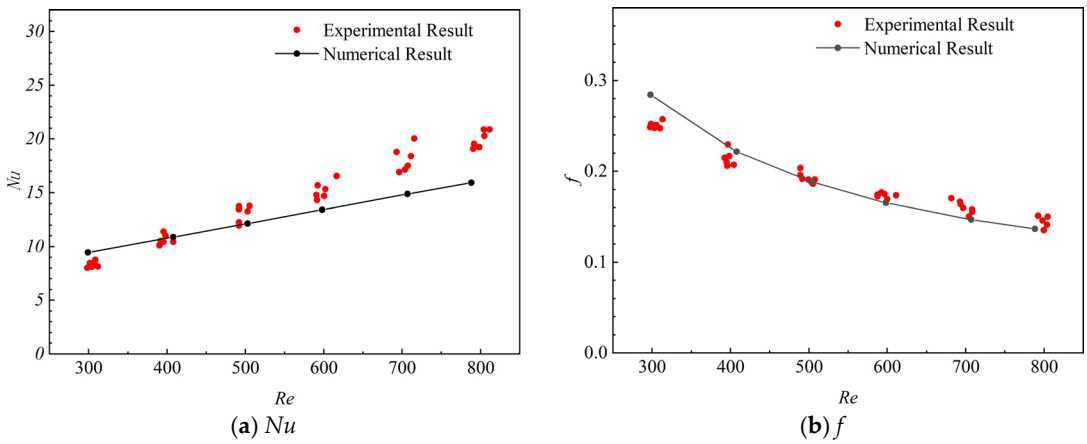

Figure 4. Comparison of the current computational model with the experimental results of Sui et al. [6]: (**a**) Nusselt number, (**b**) friction factor.

3. Results and Discussion

3.1. Global and Local Heat Transfer and Flow Characteristics

3.1.1. Local Heat Transfer and Flow Characteristics

To investigate the differences in flow characteristics between the two types of channels, the variation in velocity and static pressure difference at each vertical crest and trough along the flow direction was studied for both the conventional wavy channel and the bidirectional curved wavy microchannel with A_2 = 2 mm and λ_2 = 12 mm at an inlet velocity of 0.6 m/s, as shown in Figure 5. The cross-sectional positions considered are illustrated in Figure 6. The velocity variation trends of the two channels are generally similar, with velocity peaks occurring at positions such as x = 12, 24, 36 mm, etc. For the conventional wavy channel, these positions correspond to the horizontal crests and troughs, where the flow velocity at the throat sections (sections B and D) between adjacent horizontal crests is lower than that at the crest and trough locations. For the bidirectional

curved wavy microchannel, however, these positions correspond not only to the horizontal crests and troughs but also to the superimposed vertical troughs. As the fluid flows from the vertical crest to the vertical trough, the flow velocity increases significantly. Along the flow direction, the static pressure difference in both channels increases continuously, and the static pressure difference in the bidirectional curved wavy microchannel is consistently higher, with a faster rate of increase. The top-view pressure contours of the two channels are shown in Figure 7.

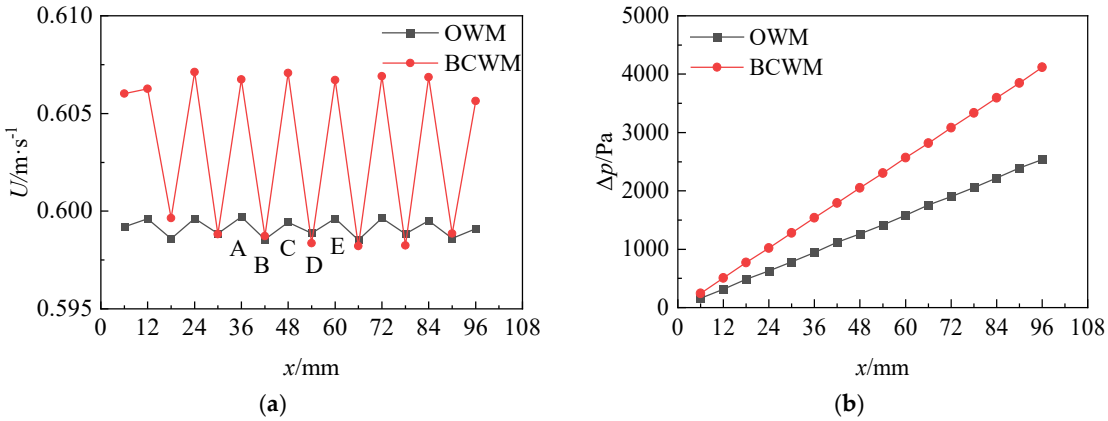

Figure 5. The distributions of flow velocity and static pressure difference in the two channels are illustrated. (**a**) Flow velocity; (**b**) static pressure difference.

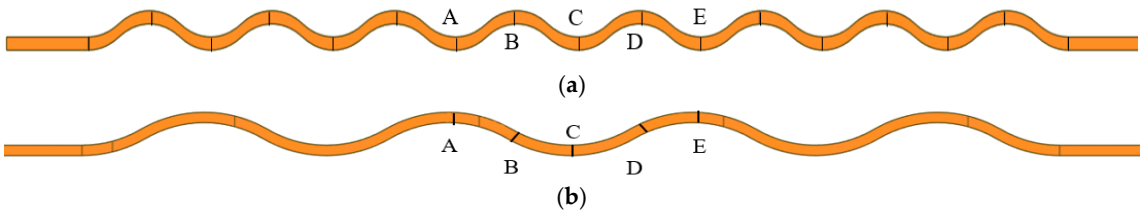

Figure 6. Schematic diagram of the cross-sectional positions. (**a**) Front view of the bidirectional curved wavy microchannel; (**b**) top views of the two microchannels.

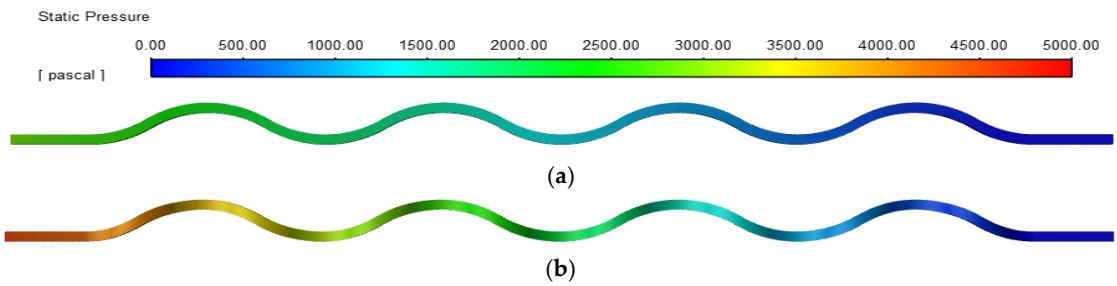

Figure 7. Pressure contours of the two channels. (**a**) OWM; (**b**) BCWM.

To investigate the differences in heat transfer characteristics between the two types of channels, the fluid temperature, coupled wall temperature, and Nusselt number at each vertical crest and trough along the flow direction were examined, as shown in Figure 8. The variation trends of fluid temperature in the two channels are generally consistent. The coupled wall temperature increases rapidly in the inlet section due to the inlet effect. Subsequently, in the middle heating section, the temperature rises in a fluctuating manner. In the outlet section, the wall temperature gradually decreases as heat is conducted through the wall to the downstream unheated low-temperature straight-channel region. The coupled wall temperature of the ordinary wavy microchannel (OWM) is significantly higher than that of the bidirectional curved wavy microchannel (BCWM). The temperature contours of the two channels

presented in Figure 9 clearly corroborate this finding. The Nusselt number of the bidirectional curved wavy microchannel at different cross-sections is higher than that of the ordinary wavy microchannel. For the ordinary wavy microchannel, the Nusselt number at the horizontal crest and trough sections (sections A, C, and E) is lower than that at the throat sections between the horizontal crests and troughs (sections B and D), which is opposite to the variation pattern of flow velocity. In contrast, the Nusselt number of the bidirectional curved wavy microchannel exhibits more pronounced fluctuations at the selected cross-sections, and its variation trend is consistent with that of the flow velocity.

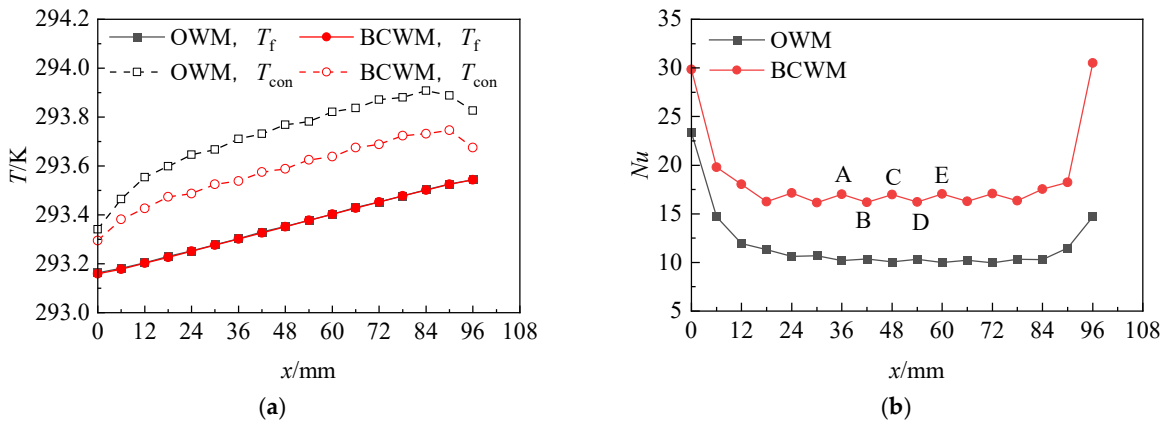

Figure 8. Distributions of fluid temperature, wall temperature, and Nusselt number for the two channels. (**a**) Temperature; (**b**) Nusselt number.

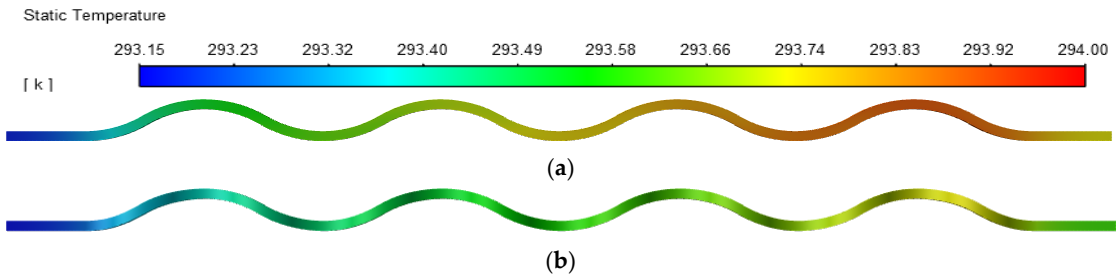

Figure 9. Coupled wall temperature contours of the two channels. (**a**) OWM; (**b**) BCWM.

3.1.2. Global Heat Transfer and Flow Characteristics

To investigate the effect of λ_2 on the heat transfer and flow characteristics of bidirectional curved wavy microchannels, microchannels with $A_2 = 2$ mm and λ_2 values of 8 mm, 12 mm, 16 mm, and 24 mm were constructed. Their front views are shown in Figure 10.

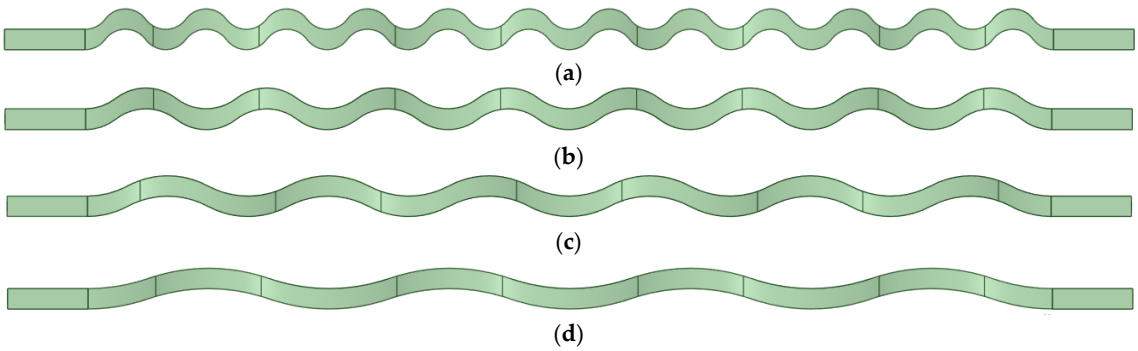

Figure 10. Front views of the fluid domains of the bidirectional curved wavy microchannels with different wavelengths λ_2. (**a**) $A_2 = 2$ mm, $\lambda_2 = 8$ mm; (**b**) $A_2 = 2$ mm, $\lambda_2 = 12$ mm; (**c**) $A_2 = 2$ mm, $\lambda_2 = 16$ mm; (**d**) $A_2 = 2$ mm, $\lambda_2 = 24$ mm.

Figure 11a,b show that the bidirectional curved wavy microchannels exhibit higher Nusselt numbers and friction factors than the ordinary wavy microchannel, while both parameters decrease with increasing λ_2. As shown in Figure 11c, the comprehensive performance factor (η) of all bidirectional curved wavy microchannels remains above 1, indicating superior overall performance. Moreover, η decreases with increasing λ_2 and reaches its maximum at an inlet velocity of 0.6 m/s for λ_2 = 8–16 mm, whereas the optimum velocity shifts to 0.8 m/s when λ_2 = 24 mm.

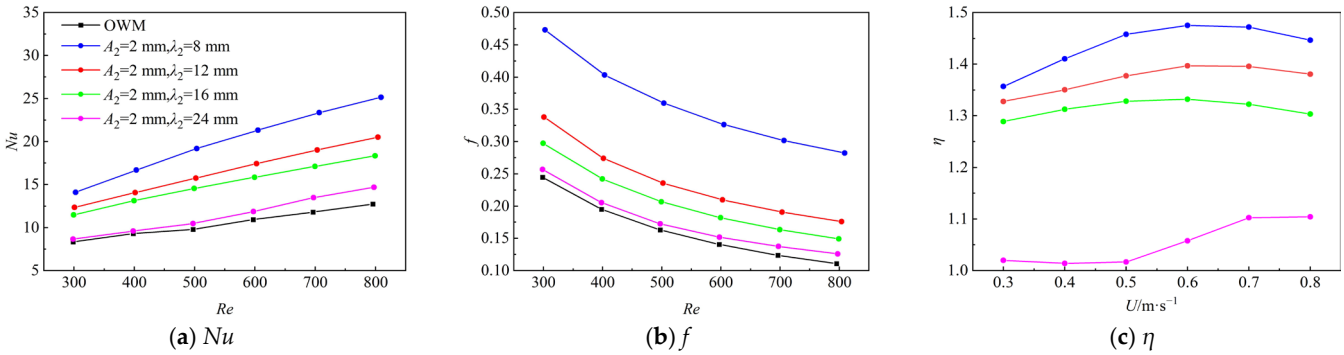

(**a**) *Nu* (**b**) *f* (**c**) η

Figure 11. Thermo-hydraulic performance of bidirectional curved wavy microchannels with the same A_2: (**a**) Nusselt number, (**b**) friction factor and (**c**) comprehensive performance factor.

To study the heat transfer and flow characteristics of bidirectional curved wavy microchannels with the same γ_2 but different A_2 and λ_2, four sets of microchannels were added with γ_2 = 4 for the following combinations: A_2 = 2 mm, λ_2 = 8 mm; A_2 = 3 mm, λ_2 = 12 mm; A_2 = 4 mm, λ_2 = 16 mm; A_2 = 6 mm, λ_2 = 24 mm; and A_2 = 8 mm, λ_2 = 32 mm. Their front views are shown in Figure 12.

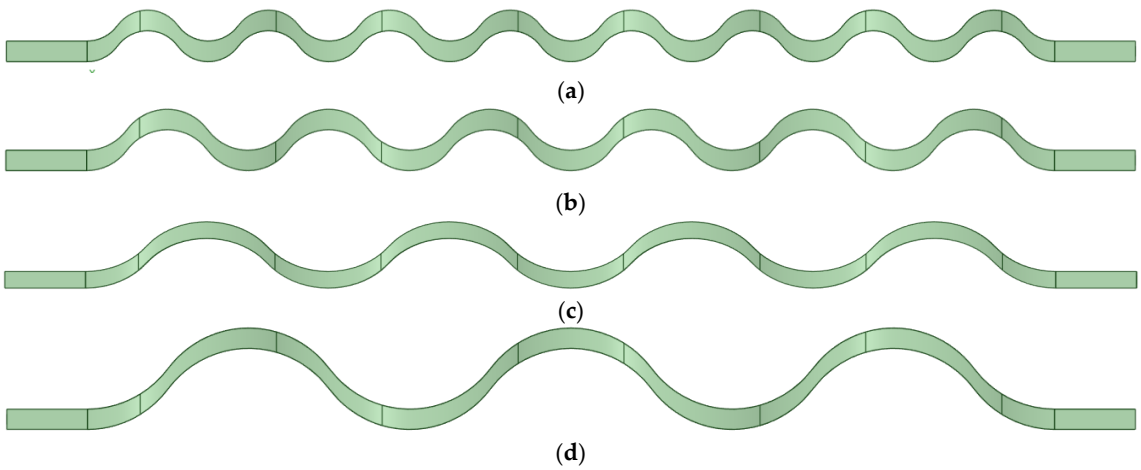

Figure 12. Front views of the fluid domains of the bidirectional curved wavy microchannels with the same wavelength-to-amplitude ratio γ_2. (**a**) A_2 = 3 mm, λ_2 = 12 mm; (**b**) A_2 = 4 mm, λ_2 = 16 mm; (**c**) A_2 = 6 mm, λ_2 = 24 mm; (**d**) A_2 = 8 mm, λ_2 = 32 mm.

From Figure 13a,b, it can be observed that the bidirectional curved wavy microchannel with A_2 = 2 mm and λ_2 = 8 mm has the highest heat transfer performance and flow resistance, while the microchannel with A_2 = 6 mm and λ_2 = 24 mm exhibits the lowest heat transfer performance and flow resistance. Notably, heat transfer performance and flow resistance do not always decrease as A_2 or λ_2 increase under the same γ_2. For instance, the heat transfer performance and flow resistance of the microchannel with A_2 = 6 mm and λ_2 = 24 mm increase when A_2 is further increased to 8 mm and λ_2 to 32 mm. From Figure 13c, the bidirectional curved wavy microchannel with A_2 = 2 mm and λ_2 = 8 mm demonstrates

the best comprehensive performance, with a maximum value achieved at an inlet velocity of 0.6 m/s.

These results indicate that the heat transfer and flow characteristics of bidirectional curved wavy microchannels with varying A_2 and λ_2 do not follow a simple geometric variation pattern for a constant γ_2. Zhu et al. [25] also mentioned that the amplitude ratio has not been proven to satisfy the similarity criterion. In other words, for a fixed amplitude ratio, different combinations of wavelength and amplitude can lead to distinct flow and heat transfer characteristics.

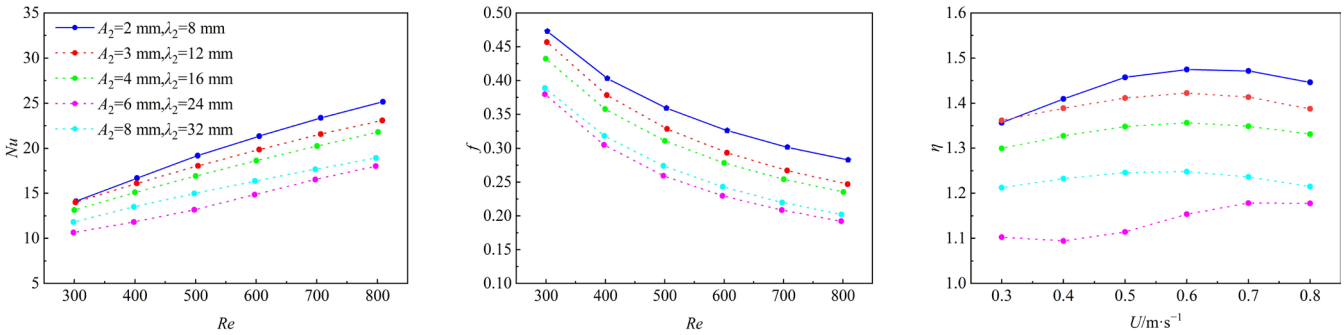

(**a**) *Nu* (**b**) *f* (**c**) η

Figure 13. Thermo-hydraulic performance of bidirectional curved wavy microchannels with the same γ_2: (**a**) Nusselt number, (**b**) friction factor and (**c**) comprehensive performance factor.

Additionally, the heat transfer and flow characteristics of bidirectional curved wavy microchannels with the same λ_2 but different A_2 are shown in Figures 14a and 14b, respectively, while the comprehensive performance is illustrated in Figure 14c. It is observed that for the same λ_2, both the Nusselt number and friction factor the increase as A_2 increases, leading to improved comprehensive performance.

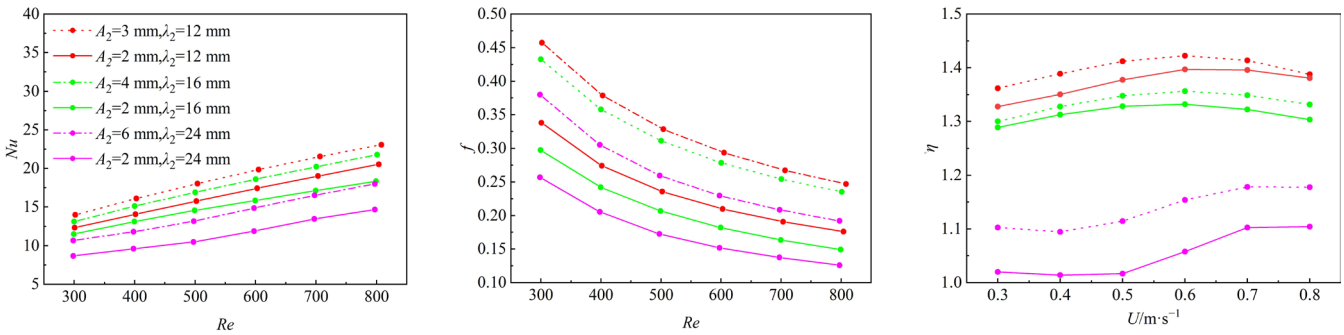

(a) *Nu* (**b**) *f* (**c**) η

Figure 14. Thermo-hydraulic performance of bidirectional curved wavy microchannels with the same λ_2: (**a**) Nusselt number, (**b**) friction factor and (**c**) comprehensive performance factor.

The effects of λ_2, A_2, and γ_2 on the heat transfer and flow characteristics of the bidirectional curved wavy microchannels were analyzed. The results indicate that *Nu*, *f*, and η are inversely proportional to γ_2, whether λ_2 or A_2 is varied to change γ_2. However, for the same γ_2, the values of *Nu*, *f*, and η do not show a direct correlation with λ_2 or A_2. Among the studied configurations, the bidirectional curved wavy microchannel with A_2 = 2 mm and λ_2 = 8 mm exhibits the best comprehensive performance at an inlet velocity of 0.6 m/s, achieving a 48% increase in η compared to the ordinary wavy microchannel. Table 1 presents the comprehensive performance factors of the studied bidirectional curved wavy microchannels.

Table 1. Comprehensive performance factors (η) of different bidirectional curved wavy microchannels at different inlet velocities.

A_2/mm	2	2	2	2	3	4	6	8
λ_2/mm	8	12	16	24	12	16	24	32
0.3 m/s	1.36	1.33	1.29	1.02	1.36	1.30	1.10	1.21
0.4 m/s	1.41	1.35	1.31	1.01	1.39	1.33	1.09	1.23
0.5 m/s	1.46	1.38	1.33	1.02	1.41	1.35	1.11	1.25
0.6 m/s	1.48	1.40	1.33	1.06	1.42	1.36	1.15	1.25
0.7 m/s	1.47	1.40	1.32	1.10	1.41	1.35	1.18	1.24
0.8 m/s	1.45	1.38	1.30	1.10	1.39	1.33	1.18	1.21

3.2. Mechanistic Analysis of Secondary Flow Effects on Heat Transfer and Flow Characteristics

To better understand the local characteristics of microchannels, the concept of secondary flow is introduced. Secondary flow refers to the transverse flow of fluid in a direction perpendicular to the main flow, caused by centrifugal forces during fluid motion. The most typical example of secondary flow is the rotational motion of fluid around an axis, known as a vortex. The fundamental physical quantity underlying various forms of vortices is vorticity, as all types of vortices are essentially collections of vorticities. The vorticity field ω is defined as the curl of the fluid velocity U $(u,\ v,\ w)$:

$$\omega = \nabla \times U = \omega_x \mathbf{i} + \omega_y \mathbf{j} + \omega_z \mathbf{k} = \begin{vmatrix} \mathbf{i} & \mathbf{j} & \mathbf{k} \\ \frac{\partial}{\partial x} & \frac{\partial}{\partial y} & \frac{\partial}{\partial z} \\ u & v & w \end{vmatrix} \tag{20}$$

The vorticity components in different directions are denoted by ω_x, ω_y and ω_z, respectively:

$$\omega_x = \frac{\partial w}{\partial y} - \frac{\partial v}{\partial z}, \omega_y = \frac{\partial u}{\partial z} - \frac{\partial w}{\partial x}, \omega_z = \frac{\partial v}{\partial x} - \frac{\partial u}{\partial y} \tag{21}$$

When the main flow is oriented in the x direction, the vorticity component along that direction depends on the gradients of the velocity components u and v in the cross-section normal to the flow:

$$\omega_x = \frac{\partial w}{\partial y} - \frac{\partial v}{\partial z} \tag{22}$$

In references [30–32], the mean value of the absolute vortex flux in the main flow direction is defined to describe the secondary flow intensity induced by the longitudinal vortex:

$$J_{\mathrm{ABS}}^{n} = \frac{1}{A} \int_A \mid \omega^{\mathrm{n}} \mid dA \tag{23}$$

Dimensionless number of the secondary flow intensity (Se) [33]:

$$Se = \frac{\rho_f \mathrm{D} U_{\mathrm{s}}}{\mu}, U_{\mathrm{s}} = \mathrm{D} J_{\mathrm{ABS}}^{\mathrm{n}} \tag{24}$$

In the Re definition, U is the main flow velocity, while in the Se definition, U_{s} is the secondary flow velocity. *Re* quantifies the ratio of inertial to viscous forces arising from the main flow, characterizing its behavior. *Se* similarly quantifies this ratio for the secondary flow, revealing its distinct characteristics.

Figure 15 presents the secondary flow intensity at sections A to E for the ordinary wavy microchannel and the bidirectional curved wavy microchannel with A_2 = 2 mm and λ_2 = 12 mm at an inlet velocity of 0.6 m/s. Compared with the ordinary wavy microchannel, the secondary flow intensity in the bidirectional curved wavy microchannel is significantly higher due to the additional vertical undulation imposed on the fluid. At the selected sections, the average secondary flow intensity in the bidirectional curved wavy microchannel with A_2 = 2 mm and λ_2 = 12 mm is increased by 153%.

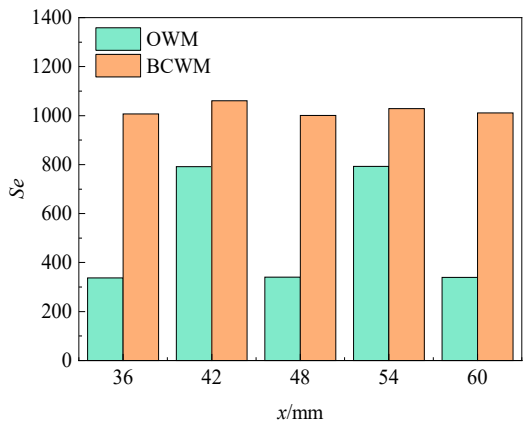

Figure 15. Secondary flow intensity distributions of the two channels.

3.3. Entropy Generation

In several studies [16,34,35], the performance of microchannel heat sinks is assessed by analyzing entropy generation. The convective heat transfer and fluid flow processes in microchannels result in variations in temperature and pressure, leading to entropy generation. Lower entropy generation signifies better energy utilization.

$$S_{\text{gen}} = S_{\text{gen,f}} + S_{\text{gen.T}} \tag{25}$$

where $S_{\text{gen.T}}$ represents the entropy generation due to heat transfer and $S_{\text{gen,f}}$ denotes the entropy generation caused by frictional pressure drop, given by the following equations [34]:

$$S_{\text{gen,T}} = \frac{q_w A_w (T_w - T_a)}{T_w T_a} \tag{26}$$

$$S_{\text{gen,f}} = \frac{q_m \Delta p}{\rho T_a} \tag{27}$$

where T_a represents the ambient temperature, which is assumed to be the inlet fluid temperature in this study.

Figure 16 illustrates the variation in the total entropy generation with Reynolds number for BCWMs with different combinations of amplitude and wavelength. For the BCWM with A_2 = 2 mm and λ_2 = 24 mm, as well as the OWM, the total entropy generation first decreases and then increases with increasing Reynolds number. In contrast, the total entropy generation rates of the other BCWM configurations increase monotonically with Reynolds number. This behavior is mainly attributed to the rapid increase in frictional entropy generation as Reynolds number increases, which gradually becomes the dominant contributor to the total entropy generation.

When $Re > 600$, the total entropy generation rates of all BCWMs exceed those of the OWM, whereas for $Re < 300$, all BCWMs exhibit lower total entropy generation rates than the OWM. At $Re \approx 300$, the total entropy generation of the OWM is 11.2% higher than that of the BCWM with A_2 = 2 mm and λ_2 = 8 mm. However, at $Re \approx 800$, the total entropy generation of the OWM becomes 53.9% lower than that of the same BCWM.

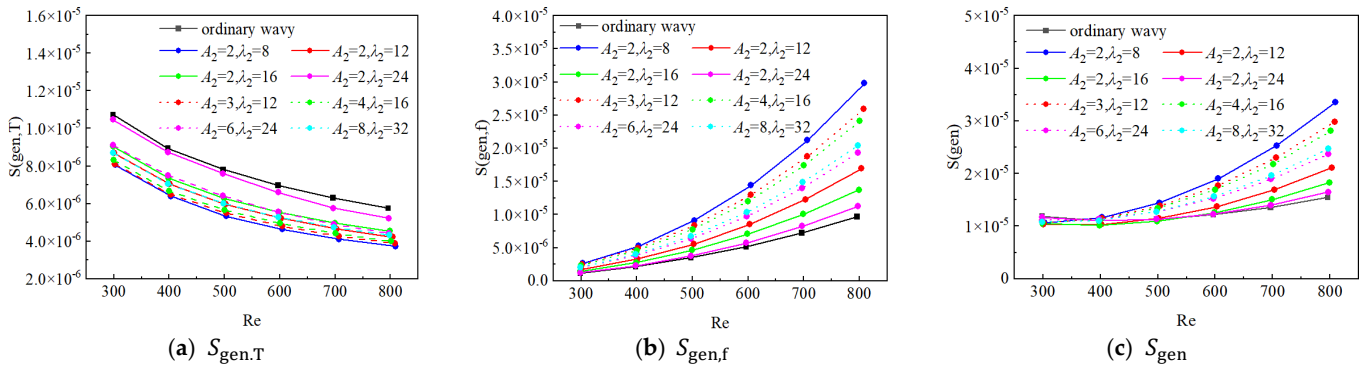

(**a**) $S_{\text{gen.T}}$ (**b**) $S_{\text{gen,f}}$ (**c**) S_{gen}

Figure 16. Entropy generation analysis of microchannels with different types as a function of Reynolds number. (**a**) Heat transfer entropy generation, (**b**) fluid flow entropy generation and (**c**) total entropy generation.

It should be noted that the comprehensive performance factor and entropy generation analysis assess enhanced heat transfer structures from different perspectives. The comprehensive performance factor is an engineering performance indicator that evaluates the trade-off between heat transfer enhancement and pressure-drop penalty under constant-pumping-power conditions. A comprehensive performance factor value greater than unity indicates that the heat transfer benefit outweighs the additional hydraulic resistance. In contrast, entropy generation analysis is based on the second law of thermodynamics and quantifies the irreversibility associated with heat transfer and fluid flow processes. Therefore, entropy generation reflects the thermodynamic quality of energy utilization rather than the overall heat transfer effectiveness.

Although both methods are governed by the balance between heat transfer enhancement and flow resistance, they emphasize different aspects of performance. Enhanced heat transfer increases the Nusselt number, thereby improving the comprehensive performance factor and reducing heat-transfer entropy generation. However, the accompanying increase in flow resistance leads to higher frictional entropy generation, which may offset the thermodynamic benefits gained from enhanced heat transfer. Consequently, comprehensive performance factor and entropy generation provide complementary, but not identical, criteria for performance evaluation. For the present BCWM, the intensified secondary flow significantly enhances heat transfer performance, resulting in comprehensive performance factor values greater than unity throughout the investigated Reynolds number range. Therefore, BCWM remains advantageous from a thermo-hydraulic performance perspective. However, at high Reynolds numbers ($Re > 600$), the rapid increase in pressure-drop-induced irreversibility causes the total entropy generation of BCWM to exceed that of the OWM. This indicates that the additional heat transfer enhancement is achieved at the expense of increased pumping-power consumption and thermodynamic losses.

Furthermore, the Reynolds number corresponding to the maximum comprehensive performance factor does not necessarily coincide with that corresponding to the minimum total entropy generation. The former represents the optimum operating condition from a thermo-hydraulic perspective, whereas the latter corresponds to the condition of maximum thermodynamic efficiency. Considering both comprehensive performance factor and entropy generation simultaneously, Reynolds numbers in the range of approximately 300–500 provide a reasonable compromise between thermal performance and thermodynamic efficiency for the BCWM configurations, since comprehensive performance factor remains greater than unity while the total entropy generation remains comparable to that of the OWM. Particularly for the BCWM with A_2 = 2 mm and λ_2 = 12 mm, at Re = 400, not only does its comprehensive performance factor reaches 1.35, but its entropy generation

also decreases by 6.87% compared with that of the OWM. This configuration achieves favorable heat transfer enhancement while reducing thermodynamic irreversibility, making it a preferred structure.

4. Conclusions

In this study, a novel three-dimensional conjugate heat transfer model for a bidirectional curved wavy microchannel (BCWM) was developed to effectively enhance heat transfer performance. The local flow and heat transfer characteristics of the BCWM and ordinary wavy microchannel (OWM) were first analyzed and compared. A dimensionless parameter, secondary flow intensity, was introduced to elucidate the underlying enhancement mechanism. Subsequently, the effects of geometric parameters, including amplitude (A_2) wavelength (λ_2), and wavelength-to-amplitude ratio (γ_2), on the overall thermo-hydraulic performance were systematically investigated. Finally, entropy generation theory was employed to evaluate the energy utilization efficiency of the microchannels. The main conclusions are summarized as follows:

(1) Compared with the OWM, the BCWM with A_2 = 2 mm and λ_2 = 8 mm significantly enhances heat transfer performance, with the comprehensive performance factor increased by up to 48%, while also resulting in a higher pressure drop. This enhancement is primarily attributed to the bidirectional curvature, which strengthens fluid disturbance and mixing.

(2) The secondary flow intensity of the preferred BCWM with A_2 = 2 mm and λ_2 = 12 mm is on average 153% higher than that of the OWM. The comprehensive performance factor reaches 1.35, and the minimum entropy generation also decreases by 6.87% at Re = 400.

(3) The thermo-hydraulic performance of the BCWM is strongly dependent on geometric parameters. Both heat transfer and flow resistance decrease with increasing wavelength. For a fixed γ_2, different combinations of A_2 and λ_2 result in significantly different performance, indicating that geometric similarity is not satisfied. Most BCWMs achieve their maximum comprehensive performance factor at an inlet velocity of 0.6 m/s.

(4) Entropy generation analysis shows that BCWM reduces heat transfer irreversibility due to enhanced thermal transport, but increases flow friction irreversibility. The total entropy generation first decreases and then increases with Reynolds number, reflecting the trade-off between heat transfer enhancement and pressure loss.

(5) This study examined whether height-direction curvature enhances heat transfer. In battery thermal management applications, horizontal wavelength and amplitude variations affect module compactness, battery–cold plate contact angle and area, and the three-dimensional internal flow path. These factors subsequently influence heat flux distribution, thermal performance, and flow resistance. Future work on BCWM-based battery thermal management will explore the coupled effects of these parameters and conduct multi-parameter multi-objective optimization.

Author Contributions: Conceptualization, J.Z., G.S. and B.W.; methodology, J.Z., G.S. and B.W.; software, J.Z.; validation, J.Z. and G.S.; formal analysis, J.Z. and G.S.; investigation, J.Z. and G.S.; resources, B.W.; data curation, J.Z. and G.S.; writing—original draft preparation, G.S.; writing—review and editing, B.W.; supervision, B.W.; project administration, B.W.; funding acquisition, B.W. All authors have read and agreed to the published version of the manuscript.

Funding: This research received no external funding.

Data Availability Statement: Data will be made available on request. The data are not publicly available due to their large size and complexity of raw data generated during the study.

Conflicts of Interest: Author Jiali Zhang was employed by the company Hangzhou Join Electric Technology Co., Ltd. The remaining authors declare that the research was conducted in the absence of any commercial or financial relationships that could be construed as a potential conflict of interest.

References

1. Lin, Y.; Luo, Y.; Li, W.; Cao, Y.; Tao, Z.; Shih, T.I. Single-phase and Two-phase Flow and Heat Transfer in Microchannel Heat Sink with Various Manifold Arrangements. *Int. J. Heat Mass Transf.* **2021**, *171*, 121118. https://doi.org/10.1016/j.ijheatmasstransfer.2021.121118.
2. Deng, T.; Ran, Y.; Zhang, G.; Chen, X.; Tong, Y. Design optimization of bifurcating mini-channels cooling plate for rectangular Li-ion battery. *Int. J. Heat Mass Transf.* **2019**, *139*, 963–973. https://doi.org/10.1016/j.ijheatmasstransfer.2019.05.082.
3. Tuckerman, D.; Pease, R. High-performance heat sinking for VLSI. *IEEE Electron. Device Lett.* **1981**, *2*, 126–129. https://doi.org/10.1109/edl.1981.25367.
4. Wang, Z.; Wang, X.; Yan, W.; Duan, Y.; Lee, D.; Xu, J. Multi-parameters optimization for microchannel heat sink using inverse problem method. *Int. J. Heat Mass Transf.* **2011**, *54*, 2811–2819. https://doi.org/10.1016/j.ijheatmasstransfer.2011.01.029.
5. Sui, Y.; Teo, C.; Lee, P.; Chew, Y.; Shu, C. Fluid flow and heat transfer in wavy microchannels. *Int. J. Heat Mass Transf.* **2010**, *53*, 2760–2772. https://doi.org/10.1016/j.ijheatmasstransfer.2010.02.022.
6. Sui, Y.; Lee, P.; Teo, C. An experimental study of flow friction and heat transfer in wavy microchannels with rectangular cross section. *Int. J. Therm. Sci.* **2011**, *50*, 2473–2482. https://doi.org/10.1016/j.ijthermalsci.2011.06.017.
7. Khoshvaght-Aliabadi, M.; Sahamiyan, M.; Hesampour, M.; Sartipzadeh, O. Experimental study on cooling performance of sinusoidal–wavy minichannel heat sink. *Appl. Therm. Eng.* **2015**, *92*, 50–61. https://doi.org/10.1016/j.applthermaleng.2015.09.015.
8. Khoshvaght-Aliabadi, M.; Feizabadi, A.; Nouri, M. Design of novel geometries for minichannels to reduce junction temperature of heat sinks and enhance temperature uniformity. *Appl. Therm. Eng.* **2021**, *192*, 116926. https://doi.org/10.1016/j.applthermaleng.2021.116926.
9. Lin, L.; Zhao, J.; Lu, G.; Wang, X.; Yan, W. Heat transfer enhancement in microchannel heat sink by wavy channel with changing wavelength/amplitude. *Int. J. Therm. Sci.* **2017**, *118*, 423–434. https://doi.org/10.1016/j.ijthermalsci.2017.05.013.
10. Sui, Y.; Teo, C.; Lee, P. Direct numerical simulation of fluid flow and heat transfer in periodic wavy channels with rectangular cross-sections. *Int. J. Heat Mass Transf.* **2011**, *55*, 73–88. https://doi.org/10.1016/j.ijheatmasstransfer.2011.08.041.
11. Gong, L.; Kota, K.; Tao, W.; Joshi, Y. Parametric numerical study of flow and heat transfer in microchannels with wavy walls. *J. Heat Transf.* **2011**, *133*, 051702. https://doi.org/10.1115/1.4003284.
12. Mohammed, H.; Gunnasegaran, P.; Shuaib, N. Numerical simulation of heat transfer enhancement in wavy microchannel heat sink. *Int. Commun. Heat Mass Transf.* **2010**, *38*, 63–68. https://doi.org/10.1016/j.icheatmasstransfer.2010.09.012.
13. Hasis, F.B.A.; Krishna, P.M.; Aravind, G.; Deepu, M.; Shine, S. Thermo hydraulic performance analysis of twisted sinusoidal wavy microchannels. *Int. J. Therm. Sci.* **2018**, *128*, 124–136. https://doi.org/10.1016/j.ijthermalsci.2018.02.018.
14. Zheng, Z.; Fletcher, D.F.; Haynes, B.S. Laminar heat transfer simulations for periodic zigzag semicircular channels: Chaotic advection and geometric effects. *Int. J. Heat Mass Transf.* **2013**, *62*, 391–401. https://doi.org/10.1016/j.ijheatmasstransfer.2013.02.073.
15. Mohammed, H.; Gunnasegaran, P.; Shuaib, N. Influence of channel shape on the thermal and hydraulic performance of microchannel heat sink. *Int. Commun. Heat Mass Transf.* **2011**, *38*, 474–480. https://doi.org/10.1016/j.icheatmasstransfer.2010.12.031.
16. Sharma, A.; Khan, M.K. Heat transfer and flow characteristics of varying curvature wavy microchannels. *Int. J. Therm. Sci.* **2023**, *185*, 108096. https://doi.org/10.1016/j.ijthermalsci.2022.108096.
17. Wang, G.; Vanka, S. Convective heat transfer in periodic wavy passages. *Int. J. Heat Mass Transf.* **1995**, *38*, 3219–3230. https://doi.org/10.1016/0017-9310(95)00051-a.
18. Ghaedamini, H.; Lee, P.; Teo, C. Developing forced convection in converging–diverging microchannels. *Int. J. Heat Mass Transf.* **2013**, *65*, 491–499. https://doi.org/10.1016/j.ijheatmasstransfer.2013.06.036.
19. Ramgadia, A.G.; Saha, A.K. Numerical study of fully developed flow and heat transfer in a wavy passage. *Int. J. Therm. Sci.* **2013**, *67*, 152–166. https://doi.org/10.1016/j.ijthermalsci.2012.12.005.
20. Zhu, Q.; Wang, Z.; Zeng, J.; Wen, X.; Deng, H.; He, W.; Zhao, T. Numerical study on flow and heat transfer in a novel symmetric sinusoidal wavy microchannel heat sink with rectangular rib prisms. *Int. J. Therm. Sci.* **2024**, *197*, 108807. https://doi.org/10.1016/j.ijthermalsci.2023.108807.
21. Zhang, L.; Duan, R.; Che, Y.; Lu, Z.; Cui, X.; Wei, L.; Jin, L. A numerical analysis of fluid flow and heat transfer in wavy and curved wavy channels. *Int. J. Therm. Sci.* **2022**, *171*, 107248. https://doi.org/10.1016/j.ijthermalsci.2021.107248.

22. Hung, T.; Yan, W.; Li, W. Analysis of heat transfer characteristics of double-layered microchannel heat sink. *Int. J. Heat Mass Transf.* **2012**, *55*, 3090–3099. https://doi.org/10.1016/j.ijheatmasstransfer.2012.02.038.
23. Xie, G.; Chen, Z.; Sunden, B.; Zhang, W. Numerical predictions of the flow and thermal performance of Water-Cooled Single-Layer and Double-Layer wavy microchannel heat sinks. *Numer. Heat Transf. Part A Appl.* **2012**, *63*, 201–225. https://doi.org/10.1080/10407782.2013.730445.
24. Xie, G.; Chen, Z.; Sunden, B.; Zhang, W. Comparative study of the flow and thermal performance of Liquid-Cooled Parallel-Flow and Counter-Flow Double-Layer wavy microchannel heat sinks. *Numer. Heat Transf. Part A Appl.* **2013**, *64*, 30–55. https://doi.org/10.1080/10407782.2013.773811.
25. Zhu, J.; Li, X.; Wang, S.; Yang, Y.; Wang, X. Performance comparison of wavy microchannel heat sinks with wavy bottom rib and side rib designs. *Int. J. Therm. Sci.* **2019**, *146*, 106068. https://doi.org/10.1016/j.ijthermalsci.2019.106068.
26. Guo, J.; Liu, F.; Xu, Y.; Han, B.; Li, M. Optimization design and numerical study of Liquid-Cooling structure for cylindrical Lithium-Ion battery pack. *J. Energy Eng.* **2021**, *147* , 04021017. https://doi.org/10.1061/(asce)ey.1943-7897.0000768.
27. Tang, Z.; Min, X.; Song, A.; Cheng, J. Thermal management of a cylindrical Lithium-Ion battery module using a multichannel wavy tube. *J. Energy Eng.* **2018**, *145* , 04018072. https://doi.org/10.1061/(asce)ey.1943-7897.0000592.
28. Yogeshwar, D.; Repaka, R.; Marath, N.K. A double serpentine channel liquid cooling plate for hotspot targeted cooling of lithium-ion batteries in a battery module. *Int. J. Therm. Sci.* **2024**, *209*, 109521. https://doi.org/10.1016/j.ijthermalsci.2024.109521.
29. Webb, R. Performance evaluation criteria for use of enhanced heat transfer surfaces in heat exchanger design. *Int. J. Heat Mass Transf.* **1981**, *24*, 715–726. https://doi.org/10.1016/0017-9310(81)90015-6.
30. Chang, L.; Wang, L.; Song, K.; Sun, D.; Fan, J. Numerical study of the relationship between heat transfer enhancement and absolute vorticity flux along main flow direction in a channel formed by a flat tube bank fin with vortex generators. *Int. J. Heat Mass Transf.* **2009**, *52*, 1794–1801. https://doi.org/10.1016/j.ijheatmasstransfer.2008.09.029.
31. Song, K.W.; Wang, L.B. Relationship between heat transfer intensity and absolute vorticity flux intensity in flat tube bank fin channels with Vortex Generators. *Prog. Comput. Fluid Dyn.* **2008**, *8*, 496. https://doi.org/10.1504/pcfd.2008.021327.
32. Song, K.; Wang, L.; Sun, D. Convective Heat Transfer and Absolute Vorticity Flux along Main Flow in a Channel formed by Flat Tube Bank Fins with Vortex Generators Mounted on Both Fin Surfaces. *J. Enhanc. Heat Transf.* **2009**, *16*, 123–139. https://doi.org/10.1615/jenhheattransf.v16.i2.30.
33. Song, K.; Wang, L. The effectiveness of secondary flow produced by vortex generators mounted on both surfaces of the FIN to enhance heat transfer in a flat tube bank FIN heat exchanger. *J. Heat Transf.* **2013**, *135*, 041902. https://doi.org/10.1115/1.4023037.
34. Yuan, D.; Zhou, W.; Fu, T.; Liu, C. Experimental and numerical investigation of heat and mass transfer in non-uniform wavy microchannels. *Int. J. Therm. Sci.* **2020**, *152*, 106320. https://doi.org/10.1016/j.ijthermalsci.2020.106320.
35. Wang, Y.; Zhou, B.; Liu, Z.; Tu, Z.; Liu, W. Numerical study and performance analyses of the mini-channel with discrete double-inclined ribs. *Int. J. Heat Mass Transf.* **2014**, *78*, 498–505. https://doi.org/10.1016/j.ijheatmasstransfer.2014.06.067.

Disclaimer/Publisher's Note: The statements, opinions and data contained in all publications are solely those of the individual author(s) and contributor(s) and not of MDPI and/or the editor(s). MDPI and/or the editor(s) disclaim responsibility for any injury to people or property resulting from any ideas, methods, instructions or products referred to in the content.